Improved thermal stability of NbCoSn half-Heusler compounds via Sb doping-induced complementary point defect evolution

Jang, Kyuseon; Dey, Poulumi; Dutta, Biswanath; Son, Ji Hee; Kim, Hyungsub; Choi, Jungwoo; Berkels, Benjamin; Kim, Bongseo; Han, Jeong Woo; Scheu, Christina

DOI
10.1016/j.cej.2025.164845

Publication date
2025

Document Version
Final published version

Published in
Chemical Engineering Journal

Chemical Engineering Journal 518 (2025) 164845

Contents lists available at ScienceDirect

Chemical Engineering Journal

journal homepage: www.elsevier.com/locate/cej

Improved thermal stability of NbCoSn half-Heusler compounds via Sb doping-induced complementary point defect evolution

Kyuseon Jang [a,b], Poulumi Dey [c], Biswanath Dutta [c], Hail Park [a], Ji-Hee Son [d], Jeong-In Jang [d], Mohammed Kamran Bhat [b], Hanhwi Jang [a], Hyungsub Kim [e], Jungwoo Choi [f], Siyuan Zhang [b], Ruben Bueno Villoro [b], Benjamin Berkels [g], Bongseo Kim [d], Pyuck-Pa Choi [a], Min-Wook Oh [h], Yeon Sik Jung [a], Jeong Woo Han [i], Christina Scheu [b,*], Chanwon Jung [b,j,**]

[a] Department of Materials Science and Engineering, Korea Advanced Institute of Science and Technology (KAIST), Daejeon 34141, Republic of Korea
[b] Max Planck Institute for Sustainable Materials, Düsseldorf 40237, Germany
[c] Department of Materials Science and Engineering, Faculty of Mechanical Engineering, Delft University of Technology, Mekelweg 2, 2628 CD Delft, the Netherlands
[d] Energy Conversion Research Center, Korea Electrotechnology Research Institute (KERI), Changwon 51543, Republic of Korea
[e] Neutron Science Division, Korea Atomic Energy Research Institute (KAERI), Daejeon 34057, Republic of Korea
[f] Computational Science Research Center, Korea Institute of Science and Technology (KIST), Seoul 02792, Republic of Korea
[g] Aachen Institute for Advanced Study in Computational Engineering Science (AICES), RWTH Aachen University, Aachen 52062, Germany
[h] Department of Materials Science and Engineering, Hanbat National University, Daejeon 34158, Republic of Korea
[i] Department of Physics Education, Chonnam National University, Gwangju 61186, Republic of Korea
[j] Department of Materials Science and Engineering, Pukyong National University, Busan 48513, Republic of Korea

ARTICLE INFO

Keywords:
Thermal stability
Half-Heusler
Thermoelectric
Point defect
Atom probe tomography
Transmission electron microscopy
Neutron diffraction

ABSTRACT

The high thermal stability of a thermoelectric material, which maintains a stable conversion efficiency under prolonged heat exposure, is essential for sustainable thermoelectric applications. Despite the well-known relationship between thermal degradation and microstructural evolution, their underlying interplay remains unclear, with contradictory findings reported in the literature owing to the complex dependence of microstructural changes on the material composition. Herein, the effect of Sb doping on the thermal stability of NbCoSn half-Heusler compounds is investigated in detail by comprehensively analyzing their microstructural evolution. The results reveal that introducing 3.3 at.% Sb into NbCoSn markedly enhances the thermal stability, by preserving the lattice thermal conductivity after heat exposure. Advanced techniques, including atom probe tomography, scanning transmission electron microscopy, and neutron diffraction, show that this improvement is driven by the evolution of Sb-induced complementary point defects. Although heat exposure significantly reduces lattice disorder in intrinsic NbCoSn, $NbCoSn_{0.9}Sb_{0.1}$ retains its lattice disorder by forming alternative point defects, thereby maintaining its lattice thermal conductivity. This detailed experimental work, corroborated by ab initio calculations, highlights the pivotal role of the point defect dynamics in achieving robust thermoelectric performances in half-Heusler compounds for high-temperature applications.

1. Introduction

Thermoelectric devices, which enable the interconversion of a temperature gradient into an electric potential, have attracted huge attention for renewable energy production owing to their unique advantages, such as constant energy production regardless of weather conditions and minimal malfunction risks due to the absence of moving parts [1–5]. In addition, thermoelectric devices can operate across a wide temperature range from 100 to 1273 K, by employing specific material systems that exhibit optimal conversion efficiency within specific temperature ranges [6–8].

The performance of thermoelectric materials is generally evaluated using the dimensionless figure of merit, $= \frac{S^2\sigma}{\kappa_L+\kappa_e}T$, where S represents the Seebeck coefficient, σ is the electrical conductivity, T is the absolute

* Corresponding author.
** Corresponding author at: Pukyong National University, Busan 48513, Republic of Korea.
E-mail addresses: c.scheu@mpie.de (C. Scheu), c.jung@pknu.ac.kr (C. Jung).

https://doi.org/10.1016/j.cej.2025.164845
Received 10 February 2025; Received in revised form 21 May 2025; Accepted 12 June 2025
Available online 14 June 2025

temperature, while κ_L and κ_e denote the lattice and electronic thermal conductivities, respectively. Achieving a high zT remains a major challenge in thermoelectrics, because the key parameters S, σ, and κ_e are inherently interdependent.

Various thermoelectric materials are being actively explored for thermoelectric power generation, such as GeTe [9], Bi_2Te_3 [10], PbTe [11,12], and half-Heusler compounds [13]. Among these, half-Heusler (HH) compounds have attracted considerable interest for medium-to-high-temperature applications up to 1000 K, owing to their high thermoelectric conversion efficiency and mechanical robustness [14–19]. These materials have a general formula XYZ, where the three sites can be substituted by different elements (e. g. X = Ti, Zr, Hf, Nb; Y = Ni, Fe, Co; Z = Sn, Sb, Bi) that comply with the 18-valence electron rule [20]. Within the group of HH compounds, NbCoSn stands out as being composed of earth-abundant elements and its favorable band structure leads to a high zT [21]. To further enhance the zT of NbCoSn, several substitutional dopants (e.g., Sb, Pt, and Zr) have been previously introduced at different lattice sites, and the highest zT = 0.7 was reported for n-type Sb-doped NbCoSn at 973 K [22].

For practical applications in thermoelectric power generation, a superior thermal stability is as a crucial as high thermoelectric performance, particularly for high-temperature uses [23,24]. A high thermal stability ensures a consistent conversion output during long-term operation, which is directly related to the reliability of a thermoelectric generator. The importance of the thermal stability is due to the fact that prolonged exposure to high temperatures can induce various microstructural changes in thermoelectric materials, such as grain coarsening, precipitation, phase segregation, oxidation, and volatilization of constituent elements, all of which may lead to thermoelectric performance degradation [25–28].

While the correlation between microstructure and thermoelectric performance has been extensively studied in HH compounds, limited research has focused on the relationship between microstructural evolution caused by long-term heat exposure and resulting thermoelectric properties [14–18,20,22,23]. In addition, the reported results on the effect of long-term heat exposure on zT show inconsistencies depending on the HH compounds. For instance, Lee et al. reported a 50 % decrease in the zT value of Sb-doped (Ti,Hf)NiSn after heat treatment at 773 K for 1 week, mainly due to the reduction of Ti/Sn antisite defects [25]. Similarly, Buffon et al. observed a 20 % decrease in the zT value of NbCoSn after heat treatment at 1123 K for 1 week, and attributed it to reduced antisite defects and increased atomic ordering [26]. In contrast, Serrano-Sánchez et al. reported that the zT value of Pt-doped NbCoSn increased by 40 % after heat treatment at 1073 K for 1 week, due to grain coarsening [27,29].

These conflicting results highlight the complexity of the microstructural changes occurring during high-temperature operation, driven by their intricate correlations with the composition. This knowledge gap hinders the development of effective strategies to improve the thermal stability of HH compounds. Therefore, a comprehensive characterization of the evolution of microstructural defects is needed to reveal their impact on thermoelectric transport properties, which is an essential task for designing efficient and stable HH compounds.

In this study, we compared the thermal stabilities of NbCoSn and $NbCoSn_{0.9}Sb_{0.1}$ and elucidated the origin of thermal stability differences through multiscale microstructural characterizations. After long-term heat exposure at 973 K for 1 week, NbCoSn exhibited a significant decrease in the zT value, whereas $NbCoSn_{0.9}Sb_{0.1}$ showed high stability. To understand this different behavior, we employed aberration-corrected scanning transmission electron microscopy (STEM) and atom probe tomography (APT) to examine the structure and local chemistry of the bulk specimens [30–32]. The results suggest that different variations in point defect evolution during long-term heat exposure contribute to the different trends of the thermoelectric properties of NbCoSn and $NbCoSn_{0.9}Sb_{0.1}$ specimens, whereas grain growth, nanoprecipitates, and grain boundary chemistry only play minor roles. Our hypothesis was validated through Rietveld refinement of neutron diffraction data and density functional theory (DFT) calculations using the Debye–Callaway model. This work enhances our understanding of process–structure–stability relationships in HH compounds, providing valuable insights for the design of HH materials with enhanced performance and thermal stability.

2. Results and discussion

2.1. Microstructural evolution via heat treatment

We first conducted X-ray diffraction (XRD) analyses of NbCoSn and $NbCoSn_{0.9}Sb_{0.1}$ to investigate the structural changes induced by heat treatment. The XRD patterns of all specimens were matched well with the cubic NbCoSn HH phase (PDF 00–052-0908), and no secondary phases were observed after heat treatment (Fig. 1a). $NbCoSn_{0.9}Sb_{0.1}$ exhibited a smaller lattice parameter than NbCoSn, as indicated by the peak shift toward higher angles in the magnified XRD patterns (Fig. 1a). Given the similar atomic radii of Sn (145 pm) and Sb (145 pm) [33], this lattice contraction is likely due to the point defects, such as vacancy formation or the removal of interstitials induced by Sb, rather than to the substitution of Sn by Sb [34]. After heat treatment, both specimens showed a slight decrease in lattice parameters (Fig. 1b), which may also be attributed to the formation or modification of lattice defects. The absence of secondary phases in the XRD patterns and the changes in the lattice parameters suggest that the heat treatment caused structural changes at the atomic scale, rather than macroscale phase transformations.

These microstructural changes were further explored using scanning electron microscopy (SEM). The SEM surface images revealed grain growth in both specimens following heat treatment, with significant differences in grain size (Fig. 1c–f). The average grain sizes of the as-sintered NbCoSn (140 ± 10 nm) and $NbCoSn_{0.9}Sb_{0.1}$ (150 ± 20 nm) specimens were nearly identical. However, after heat treatment, the grain size of NbCoSn (430 ± 90 nm) became markedly larger than that of $NbCoSn_{0.9}Sb_{0.1}$ (270 ± 40 nm). This difference can be attributed to the solute drag effect caused by Sb atoms inhibiting grain boundary movement during heat treatment. A similar inhibition of grain growth by dopants has been reported for other systems, such as Bi_2Te_3 and $Si_{80}Ge_{20}$ [8,35]. Although no distinct secondary phases were detected by XRD, energy-dispersive X-ray spectroscopy (EDS) in the SEM revealed the formation of Co-rich grains in both heat-treated specimens, while the as-sintered specimens showed a homogeneous elemental distribution (Fig. S1). The SEM-EDS results also revealed similar Nb concentrations with a slight excess of Co for the as-sintered NbCoSn and $NbCoSn_{0.9}Sb_{0.1}$ specimens (Table S1). This Co excess is consistent with previous reports on NbCoSn materials synthesized via high-temperature techniques [27,36–38]. The compositions of NbCoSn and $NbCoSn_{0.9}Sb_{0.1}$ remained the same after heat treatment.

Next, we performed STEM-EDS analyses to closely examine the Co-rich regions in both heat-treated specimens. In the heat-treated NbCoSn specimen, most Co-rich grains were located at triple junctions (Fig. 2a). The chemical composition of these Co-rich grains, determined via STEM-EDS, was approximately Co_2Nb (26.9 ± 2.2 at.% Nb; 62.7 ± 2.2 at.% Co; 10.4 ± 1.2 at.% Sn), whereas that of most grains was close to nominal NbCoSn (32.4 ± 2.5 at.% Nb; 34.5 ± 1.8 at.% Co; 33.1 ± 2.5 at.% Sn). Additionally, Co-rich precipitates were identified within the grain interiors (Fig. 2b). These precipitates showed elongated shapes along the [001] direction of the HH matrix as well as a larger lattice constant (6.20 Å) compared to NbCoSn (5.96 Å), and were only found in the grain interiors (Fig. 2c). The line concentration profile in Fig. 2d confirms that these Co-rich precipitates corresponded to the $NbCo_2Sn$ Heusler phase, consistent with their larger lattice parameter compared to the HH matrix [39].

Similarly, the heat-treated $NbCoSn_{0.9}Sb_{0.1}$ specimen showed a grain composition close to the nominal value (33.0 ± 2.5 at.% Nb; 34.3 ± 1.7

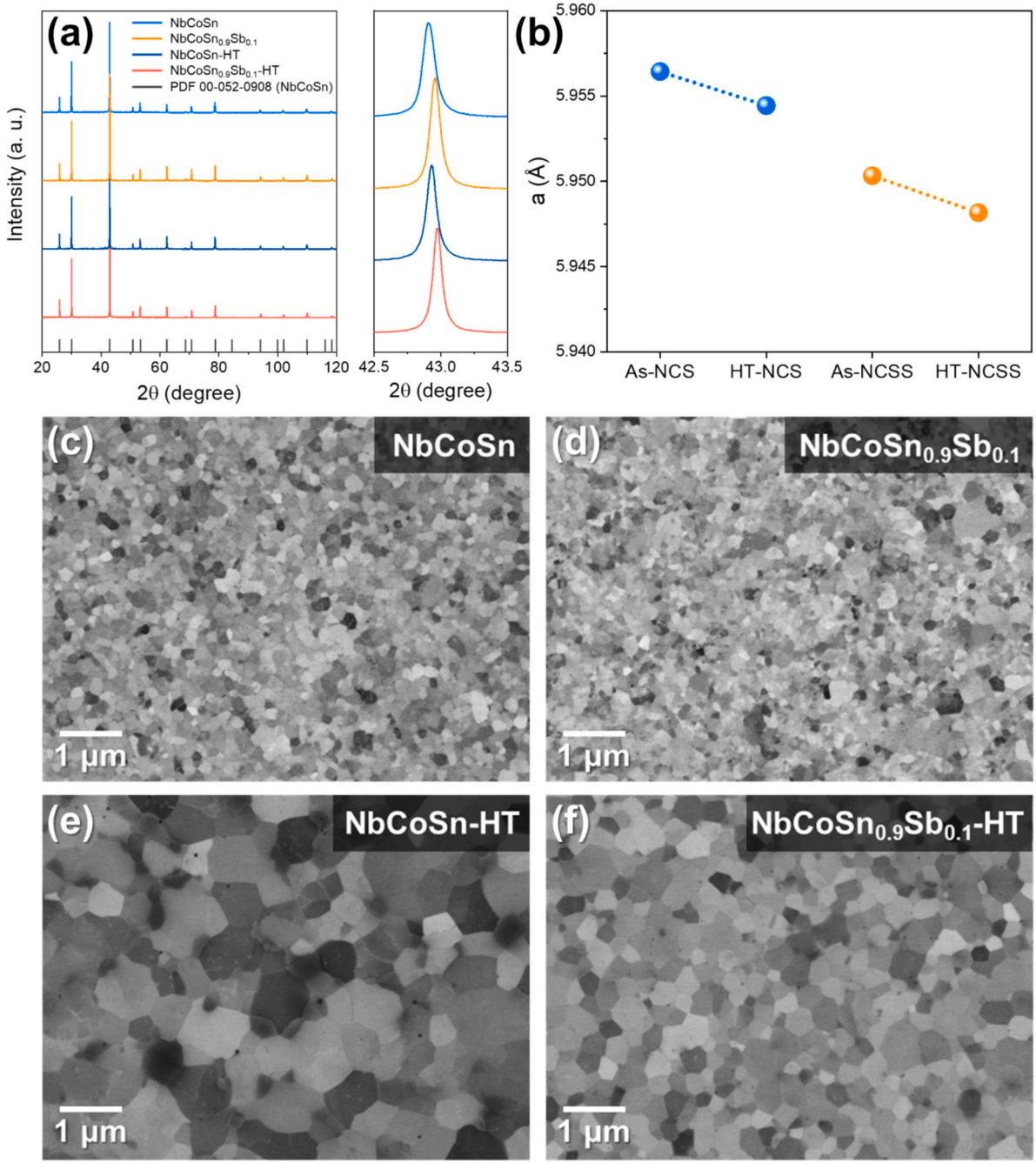

Fig. 1. Structural characterization of NbCoSn and $NbCoSn_{0.9}Sb_{0.1}$ before and after heat treatment. (a) XRD patterns of as-sintered and heat-treated NbCoSn and $NbCoSn_{0.9}Sb_{0.1}$ specimens at 973 K for 1 week. The magnified XRD patterns represent the 42.5°–43.5° range; HT denotes heat-treated specimens. (b) Lattice parameters of each specimen obtained from XRD. NCS and NCSS denote NbCoSn and $NbCoSn_{0.9}Sb_{0.1}$, respectively. (c–f) SEM images of (c,d) as-sintered and (e,f) heat-treated NbCoSn and $NbCoSn_{0.9}Sb_{0.1}$ specimens, respectively.

at.% Co; 29.0 ± 2.4 at.% Sn; 3.7 ± 0.5 at.% Sb) (Fig. 2e). Co-rich grains with a composition similar to Co_2Nb (25.5 ± 2.0 at.% Nb; 63.0 ± 1.9 at.% Co; 10.4 ± 1.0 at.% Sn; 1.1 ± 0.1 at.% Sb) were also observed at triple junctions. However, the average size of Co_2Nb grains in the heat-treated $NbCoSn_{0.9}Sb_{0.1}$ was smaller (~70 nm) than that in the heat-treated NbCoSn (~250 nm). Notably, Heusler precipitates were absent in the heat-treated $NbCoSn_{0.9}Sb_{0.1}$. This may be attributed to the inherently lower Co concentration in the HH matrix of $NbCoSn_{0.9}Sn_{0.1}$ than NbCoSn. The lower Co concentration could result in a reduced driving force for the precipitation of the $NbCo_2Sn$ Heusler phase in the grain interior of $NbCoSn_{0.9}Sb_{0.1}$.

The three-dimensional atomic distributions and accurate compositions of each specimen were determined by APT. The 3D atom map of the heat-treated NbCoSn (Fig. 3a) revealed spheroidal Nb_2Co and NbO precipitates as well as disk-shaped $NbCo_2Sn$ precipitates, with the corresponding 1D concentration profiles shown in Fig. 3b–d. The lengths of Nb_2Co and NbO obtained from the APT results were approximately 15 and 10 nm, respectively, while $NbCo_2Sn$ had a larger size (~70 nm). Larger Co_2Nb grains (~250 nm) were only observed in the STEM-EDS analysis (Fig. 2a), but not in the APT specimens, due to the limited sampling volumes (Fig. S2).

On the other hand, the 3D atom map of the heat-treated $NbCoSn_{0.9}Sb_{0.1}$ showed spheroidal Nb_2Co, NbO, and Co_2Nb precipitates (Fig. 3e–g). The size range of Nb_2Co and NbO was similar to

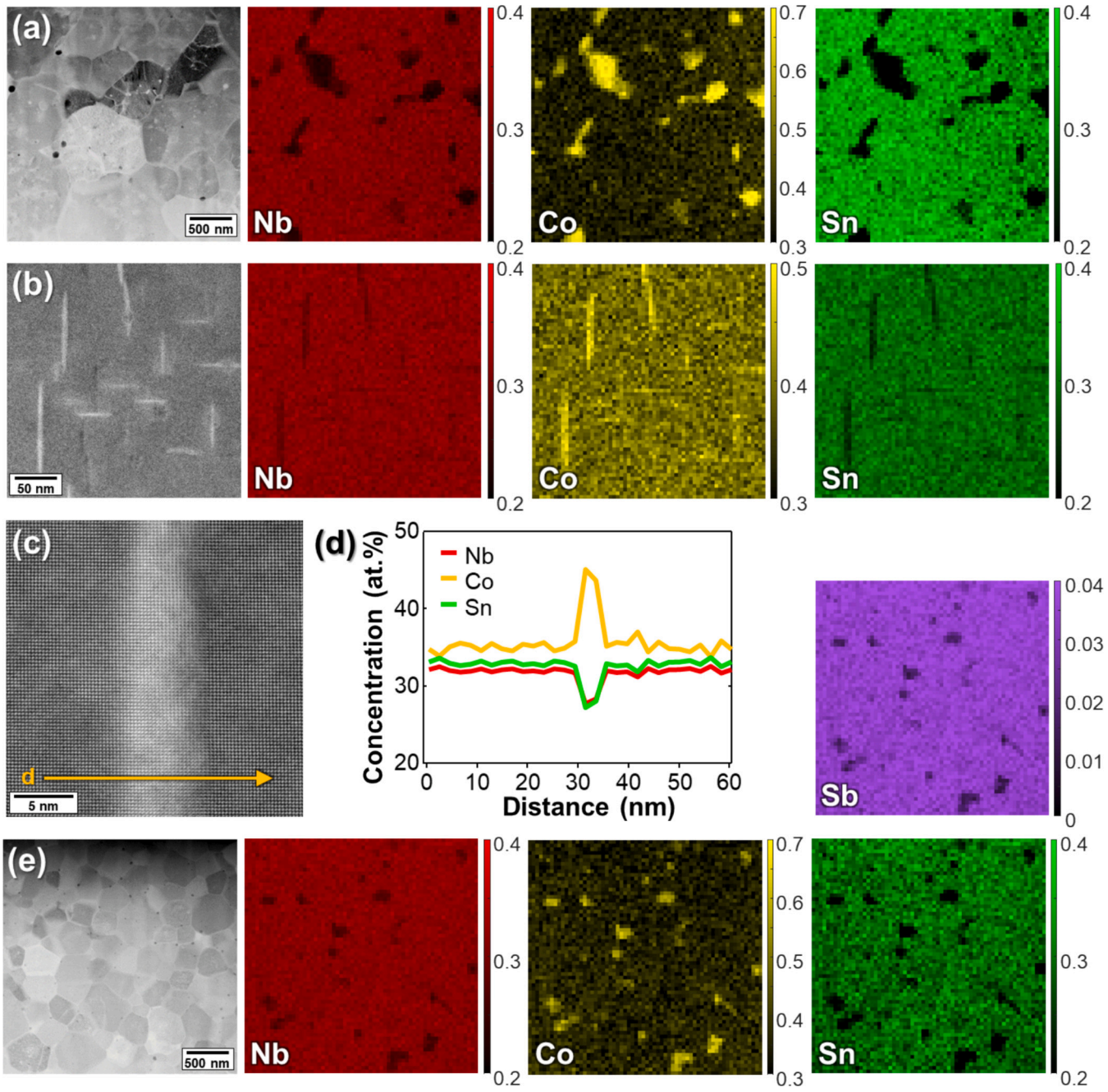

Fig. 2. STEM-EDS analysis of Co-rich precipitates in heat-treated specimens. (a,b) HAADF-STEM images with corresponding EDS maps for heat-treated NbCoSn specimen, showing (a) grain structures and (b) grain interior. (c) Magnified HAADF-STEM image of Co-rich precipitate observed in (b), and (d) line concentration profile across the precipitate, showing a composition close to Heusler phase $NbCo_2Sn$. (e) HAADF-STEM image with corresponding EDS maps for heat-treated $NbCoSn_{0.9}Sb_{0.1}$ specimen. Gradient colors and numerical values in all EDS maps represent the molar fraction of each element.

that of the heat-treated NbCoSn. In addition to the large Co_2Nb particles (~50 nm) observed in the STEM images, smaller Co_2Nb precipitates (~6 nm) were also detected in the 3D atom map (Figs. 2e and S3). These findings suggest that the small amount of Sb in $NbCoSn_{0.9}Sb_{0.1}$ may alter the types and sizes of nanoscale precipitates. To confirm the presence of nanoprecipitates, we further analyzed the as-sintered specimens using APT (Figs. S4 and S5). The 3D atom maps of both specimens revealed the presence of Nb_2Co but not Co-rich precipitates. This indicates that heat treatment induced the formation of Co-rich precipitates (i.e., Co_2Nb and $NbCo_2Sn$ in NbCoSn; Co_2Nb in $NbCoSn_{0.9}Sb_{0.1}$) while retaining Nb_2Co grains.

The matrix compositions of all specimens are shown in Fig. 3h. Both as-sintered specimens contained excess Co, attributed to the formation of energetically favorable Co interstitials [40,41]. The rapid cooling during the melt-spinning process likely maintained the system in a metastable state, facilitating the retention of Co interstitials. Although both specimens showed Co excess compositions, the measured matrix composition of the as-sintered $NbCoSn_{0.9}Sb_{0.1}$ was closer to the nominal stoichiometry ($Nb_{1.00}Co_{1.05}Sn_{0.85}Sb_{0.1}$), compared to that of the as-sintered NbCoSn ($Nb_{0.86}Co_{1.10}Sn_{1.04}$). Notably, as-sintered NbCoSn exhibits a severe Nb deficiency, indicating a high concentration of point defects at Nb sites. In contrast, $NbCoSn_{0.9}Sb_{0.1}$ did not show Nb deficiency but a slight Sn deficiency instead. This observation suggests that Sb doping may suppress the formation of Co interstitials and Nb-site defects, thereby improving the phase stability of NbCoSn by maintaining a composition closer to the stoichiometric one.

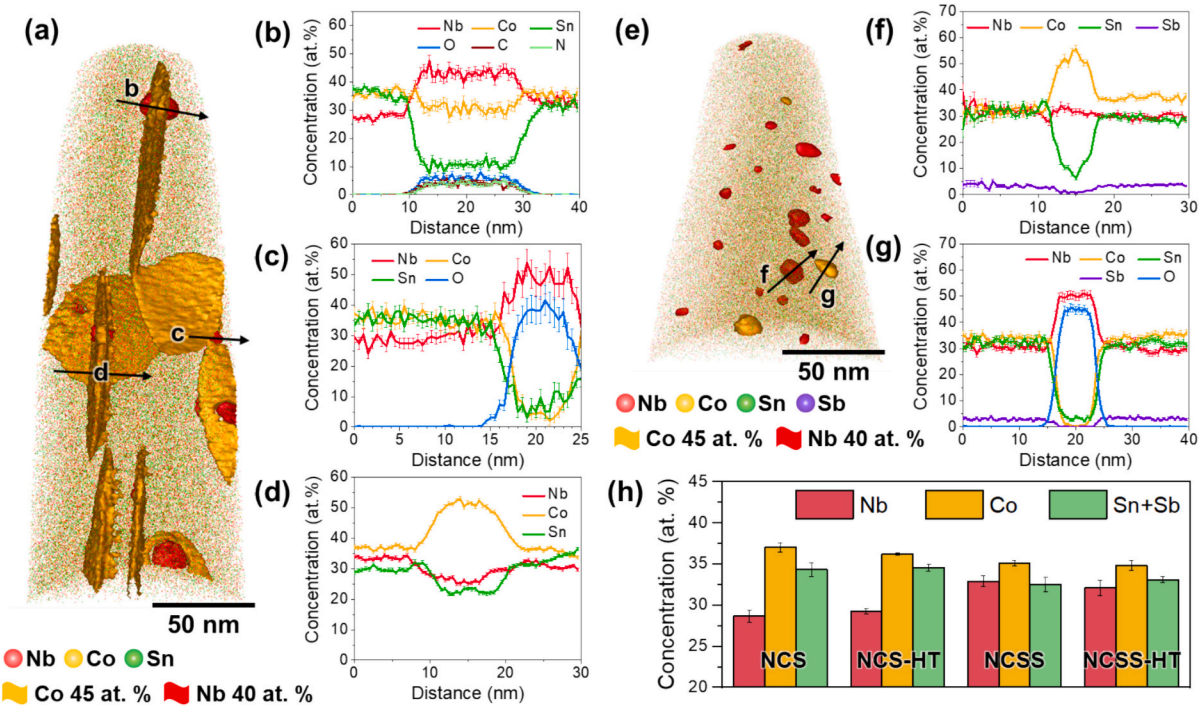

Fig. 3. APT analysis of heat-treated specimens. (a) 3D atom map of heat-treated NbCoSn with Co 45 at.% (yellow) and Nb 40 at.% (red) isoconcentration surfaces. (b–d) 1D concentration profiles across (b) Nb_2Co, (c) NbO, and (d) $NbCo_2Sn$ precipitates, as marked in (a). (e) 3D atom map of heat-treated $NbCoSn_{0.9}Sb_{0.1}$ with Co 45 at.% (yellow) and Nb 40 at.% (red) isoconcentration surfaces. (f,g) 1D concentration profiles across (f) Co_2Nb and (g) NbO precipitates, as indicated in (e). (h) Average compositions of half-Heusler matrices for NbCoSn and $NbCoSn_{0.9}Sb_{0.1}$ specimens before and after heat treatment, obtained from multiple APT datasets. (For interpretation of the references to colour in this figure legend, the reader is referred to the web version of this article.)

The initial compositional differences also affected the matrix compositions after heat treatment. The heat-treated NbCoSn remained Co-rich and Nb-deficient, although the excess Co decreased and the Nb deficiency was reduced ($Nb_{0.86}Co_{1.10}Sn_{1.04}$ → $Nb_{0.88}Co_{1.08}Sn_{1.04}$). This change was mainly due to the formation of Co-rich precipitates (Co_2Nb and $NbCo_2Sn$), driven by the excess Co in the matrix. Despite some Nb being incorporated into precipitates, the overall increase in Nb concentration in the matrix was due to the relatively small volume fraction of the Nb-rich precipitates (Nb_2Co and NbO) and the significant reduction in excess Co. In the case of heat-treated $NbCoSn_{0.9}Sb_{0.1}$, smaller amounts of precipitates were formed compared to NbCoSn, resulting in only a small change in Co concentration, with a slight Nb reduction ($Nb_{1.00}Co_{1.05}Sn_{0.85}Sb_{0.1}$ → $Nb_{0.96}Co_{1.04}Sn_{0.9}Sb_{0.1}$). The formation of Co_2Nb, Nb_2Co, and NbO resulted in the Sn concentration approaching the stoichiometric value, while that of Nb decreased.

2.2. Thermoelectric transport properties and thermal stability

The distinct microstructural evolution of NbCoSn and $NbCoSn_{0.9}Sb_{0.1}$ upon heat treatment led to differences in their thermoelectric transport properties. As-sintered $NbCoSn_{0.9}Sb_{0.1}$ showed a significantly larger electrical conductivity (σ) than as-sintered NbCoSn, due to its higher carrier concentration (n_H) and carrier mobility (μ_H) induced by Sb doping, as confirmed by Hall measurements (Fig. 4a and b). After heat treatment, the σ values of both specimens decreased with decreasing carrier concentration (Fig. 4a and b). This decrease is likely due to the elimination of Co interstitials, which was confirmed by the decrease in Co concentrations in the matrices, as Co interstitials serve as electron donors in NbCoSn by forming energy states within the bandgap.[30]

In contrast, the Seebeck coefficient (S) is inversely proportional to the carrier concentration according to the Pisarenko relation, and decreases with Sb addition [42]. At the same time, heat treatment led to an increased S in both specimens, due to the reduction in n_H (Fig. 4c). Notably, the increase in S for $NbCoSn_{0.9}Sb_{0.1}$ was marginal, despite a 50 % decrease in n_H after heat treatment. This led to a reduction in the power factor ($S^2\sigma$) of $NbCoSn_{0.9}Sb_{0.1}$ after heat treatment, while that of NbCoSn was almost unchanged (Fig. 4d).

The unconventional change in the S value for $NbCoSn_{0.9}Sb_{0.1}$ can be explained by a change in the density-of-states (DOS) effective mass (m^*). The Pisarenko plot show that as-sintered $NbCoSn_{0.9}Sb_{0.1}$ had a larger m^* ($7.4m_0$, where m_0 is the electron mass) compared to as-sintered NbCoSn ($5.6m_0$), consistent with a previous report (Fig. 4e) [21]. While the m^* value of as-sintered NbCoSn remained unchanged after heat treatment, that of $NbCoSn_{0.9}Sb_{0.1}$ decreased to $5.3m_0$, similar to that of the as-sintered NbCoSn. The substantial reduction in m^* implies a change in the band structure of $NbCoSn_{0.9}Sb_{0.1}$ following heat treatment [8], leading to a reduced power factor (Fig. 4d). To further investigate whether the observed changes in m^* originate from alterations in the band structure, we also calculated Seebeck effective mass (m_s^*) for each specimen. m_s^* provides a more direct means of probing band structure changes, as it is independent of scattering mechanisms and the microstructural factors [43]. Notably, m_s^* exhibited the same trend as m^* derived from the Pisarenko plot. Specifically, for NbCoSn, m_s^* changed only slightly from 5.6 m_0 to 5.8 m_0, whereas for $NbCoSn_{0.9}Sb_{0.1}$, m_s^* decreased significantly from 7.4 m_0 to 5.3 m_0. This consistent behavior supports that the reduction in m^* is driven by modifications in the electronic band structure.

The weighted mobility (μ_w) for each specimen was calculated to elucidate the carrier scattering mechanisms (Supplementary text and Fig. 4f). Owing to its large m^*, as-sintered $NbCoSn_{0.9}Sb_{0.1}$ showed the largest μ_w, as calculated by the following equation [44]:

$$\mu_w = \mu_H \left(\frac{m^*}{m_0}\right)^{3/2} \quad (1)$$

In NbCoSn, μ_w initially increased up to 500 K and then decreased. Such thermally-activated μ_w can be attributed to grain boundary

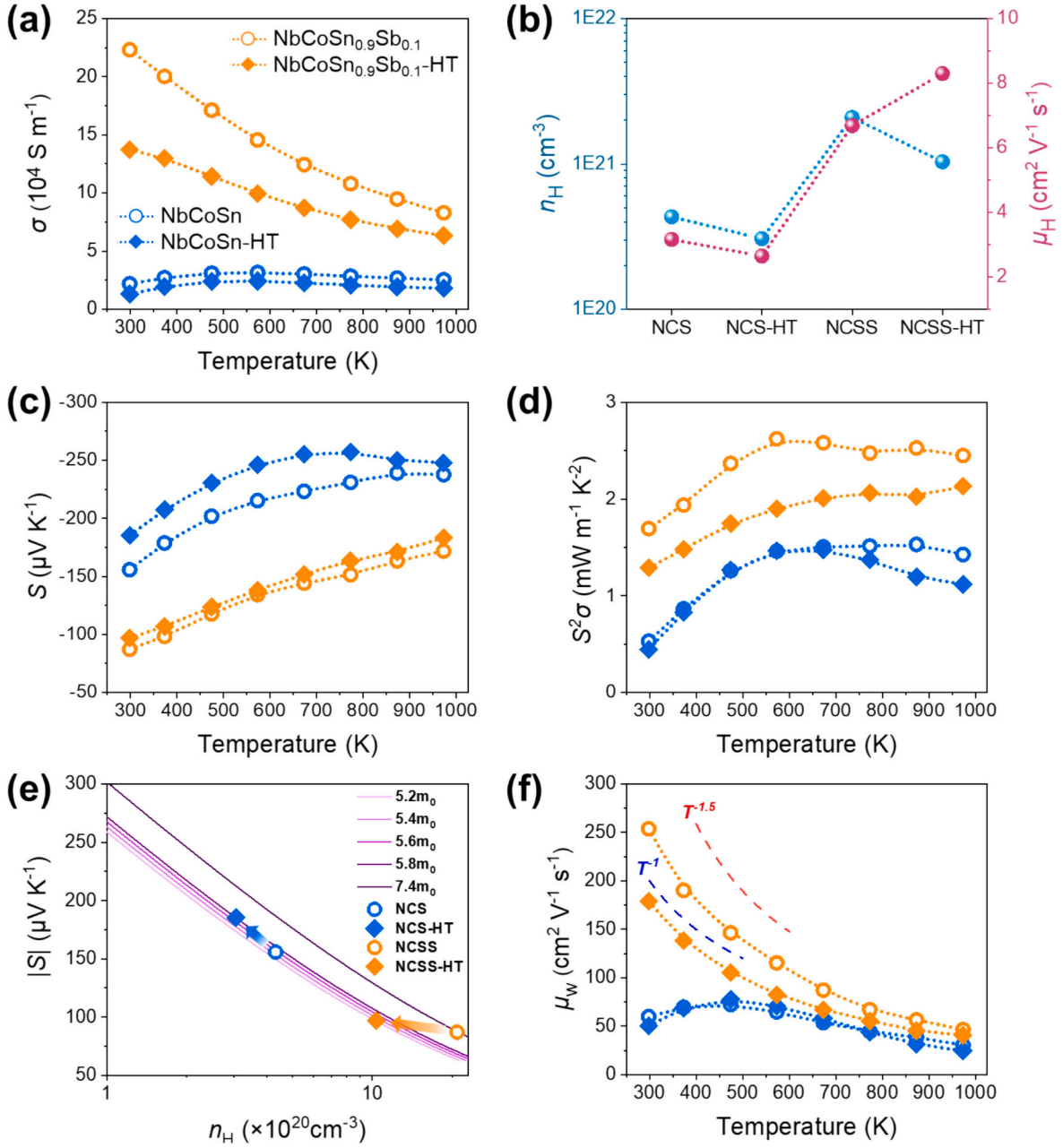

Fig. 4. Electrical transport properties. (a) Electrical conductivities, (b) Hall carrier concentrations and Hall mobilities at 300 K, (c) Seebeck coefficients, (d) power factor, (e) Pisarenko plots at 300 K using the single parabolic band model (m_0 represents the electron mass), and (f) weighted mobilities of NbCoSn and $NbCoSn_{0.9}Sb_{0.1}$ before and after heat treatment.

scattering of charge carriers due to the resistive grain boundary, as previously reported for NbCoSn [29]. In contrast, the μ_w value of as-sintered $NbCoSn_{0.9}Sb_{0.1}$ followed the temperature dependence $\mu_w \propto T^{-1.5}$. This trend indicates that acoustic phonon scattering via the deformation potential is the main carrier scattering mechanism in as-sintered $NbCoSn_{0.9}Sb_{0.1}$, whereas grain boundary scattering is effectively suppressed by Sb doping [45]. However, after heat treatment, the temperature dependence shifted to $\mu_w \propto T^{-1}$, which indicates a mixed carrier scattering mechanism involving both acoustic phonon ($T^{-1.5}$) and point defect ($T^{-0.5}$) scattering [45]. This change confirms the intensified point defect scattering mechanism in $NbCoSn_{0.9}Sb_{0.1}$ after heat treatment [45]. Therefore, we believe that point defects are responsible for the m^* change in $NbCoSn_{0.9}Sb_{0.1}$.

Along with a higher σ, as-sintered $NbCoSn_{0.9}Sb_{0.1}$ also exhibited a higher total thermal conductivity (κ_{total}) than as-sintered NbCoSn (Fig. 5a). This difference is mainly attributed to the significantly higher electronic thermal conductivity (κ_e) of as-sintered $NbCoSn_{0.9}Sb_{0.1}$, as described by the Wiedemann–Franz law (Fig. 5b):

$$\kappa_e = L\sigma T, \kappa_L = \kappa_{total} - \kappa_e \quad (2)$$

where L, T, and κ_L represent the Lorenz number, absolute temperature, and lattice thermal conductivity, respectively. The L value of each specimen was calculated by the single parabolic band model (See Supplementary Information and Fig. S6). Notably, $NbCoSn_{0.9}Sb_{0.1}$ showed a slightly higher κ_L than NbCoSn, because the small mass difference between Sb (121.8 amu) and Sn (118.7 amu) is insufficient to induce strong mass fluctuation scattering (Fig. 5c) [21].

After heat treatment, the κ_{total} of both specimens exhibited significant changes. In the case of NbCoSn, κ_{total} increased by approximately 40 %, mainly due to a substantial rise (~50 %) in κ_L (Fig. 5a and c). In contrast,

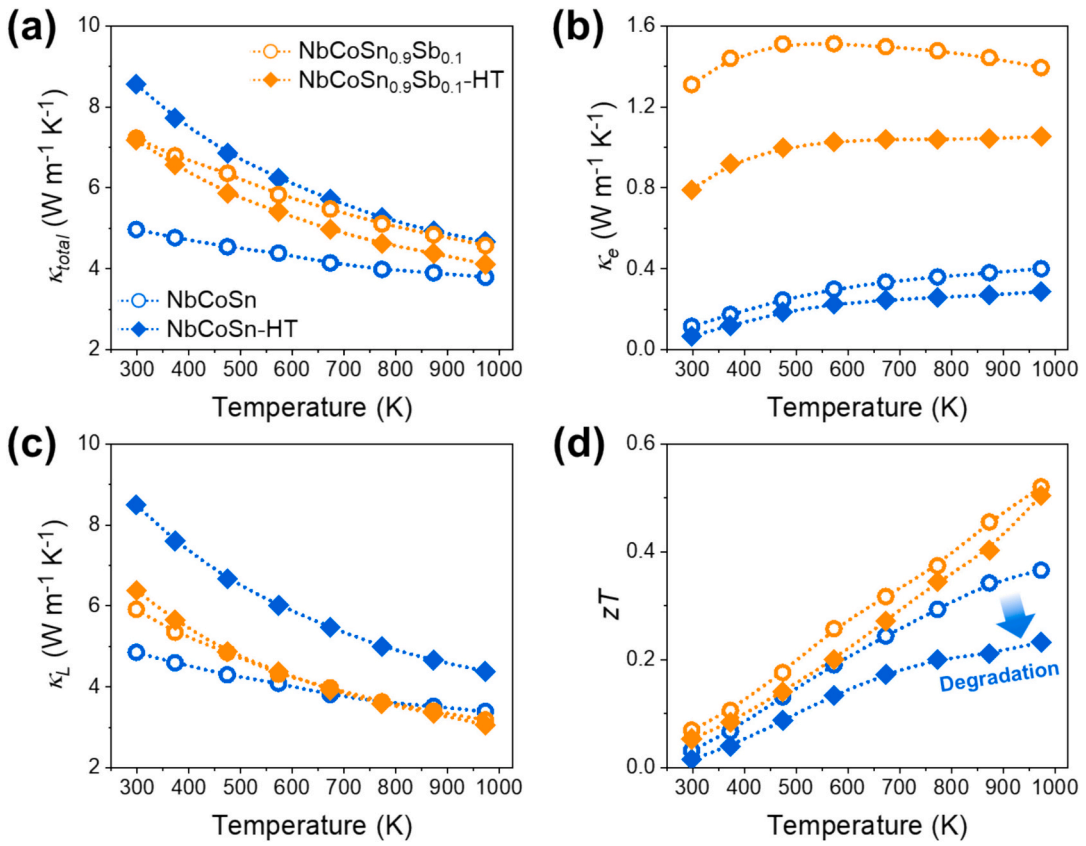

Fig. 5. Thermal transport properties and zT. (a) Total thermal conductivity (κ_{total}), (b,c) calculated electronic (κ_e) and lattice thermal conductivities (κ_L), as well as (d) figure-of-merit (zT) of NbCoSn and $NbCoSn_{0.9}Sb_{0.1}$ specimens before and after heat treatment (HT).

$NbCoSn_{0.9}Sb_{0.1}$ exhibited a slightly decreased κ_{total}, driven by a reduction in κ_e with an unchanged κ_L. While the decrease in κ_e corresponds to the observed decrease in σ, the unchanged κ_L for $NbCoSn_{0.9}Sb_{0.1}$ after heat treatment is unexpected. After heat treatment, the κ_L of $NbCoSn_{0.9}Sb_{0.1}$ was ~30 % lower than that of NbCoSn. Consequently, a notable drop (~36 %) in the zT value was observed for NbCoSn, whereas $NbCoSn_{0.9}Sb_{0.1}$ maintained an almost unchanged zT, demonstrating greater thermal stability after heat treatment at 973 K for 1 week (Fig. 5d). The enhanced thermal stability of $NbCoSn_{0.9}Sb_{0.1}$ led to a much smaller decrease in its average and peak zT values compared to NbCoSn (Fig. S7). These findings suggest that even a small addition of Sb can considerably improve the thermal stability of NbCoSn by suppressing the increase in κ_L after heat treatment.

To elucidate the origin of these results, we measured the sound velocity (v_{sound}) of both specimens before and after heat treatment, because v_{sound} is closely related to κ_L via the following relationship from kinetic gas theory [46]:

$$\kappa_L = \frac{1}{3} C_v v_{sound}^2 \tau \tag{3}$$

where C_v is the specific heat and τ is the phonon relaxation time (see Experimental section). As shown in Fig. S8a, the measured v_{sound} of $NbCoSn_{0.9}Sb_{0.1}$ decreased by 10 % after heat treatment, while that of NbCoSn remained similar. For isotropic materials, the longitudinal (v_l) and transverse (v_t) components of v_{sound} are determined by the elastic moduli and density of a specimen, according to the following relations:

$$v_l = \sqrt{\frac{B + 4G/3}{\rho}}, v_t = \sqrt{\frac{G}{\rho}} \tag{4}$$

where B, G, and ρ are the bulk modulus, shear modulus, and density, respectively. For isotropic materials, G can be calculated as $\frac{Y}{2(1+\mu)}$ (Y: Young's modulus; μ: Poisson's ratio) [47]. The v_l and v_t components of each specimen are shown in Table S2.

Because the densities of both specimens were almost unchanged after heat treatment (NbCoSn: 8.50 g cm^{-3}; $NbCoSn_{0.9}Sb_{0.1}$: 8.48 g cm^{-3}), the observed changes in v_{sound} can be attributed to variations in the elastic moduli, particularly in $NbCoSn_{0.9}Sb_{0.1}$. The B and Y values calculated using Eq. (4) showed a more significant decrease in $NbCoSn_{0.9}Sb_{0.1}$ after heat treatment (Fig. S8b and S8c), consistent with the large reduction of v_{sound} for this specimen. The Y value measured by nanoindentation also exhibited the same trend as the calculated one, confirming that heat treatment induced a noticeable softening effect in the elastic properties of $NbCoSn_{0.9}Sb_{0.1}$ (Fig. S8d).

To explore whether these variations in elastic moduli and v_{sound} stem from changes in chemical bonding, we obtained the Grüneisen parameter γ, which is a quantitative measure of bond anharmonicity. A higher γ typically corresponds to a greater lattice anharmonicity (i.e., a softened lattice), which slows down phonon propagation and leads to a lower κ_L. Because there is no universal method to calculate γ, we used two methods, based on the Poisson's ratio and the coefficient of thermal expansion (CTE), to estimate the γ values for both specimens (Fig. S9; the details are reported in the Supplementary text). Although the two methods produced slightly different γ values, they revealed a consistent trend: the γ value of NbCoSn remained relatively unchanged after heat treatment, whereas that of $NbCoSn_{0.9}Sb_{0.1}$ decreased. This reduction in γ suggests that the chemical bonds in $NbCoSn_{0.9}Sb_{0.1}$ became more harmonic after heat treatment. Given that more harmonic bonds typically result in increased elastic moduli and v_{sound} values, the observed reduction in both parameters for $NbCoSn_{0.9}Sb_{0.1}$ cannot be attributed to the change in bonding characteristics [47]; instead, other factors, such as microstructural features, are likely responsible for these variations

[48].

Furthermore, the simultaneous reductions in both v_{sound} and γ for $NbCoSn_{0.9}Sb_{0.1}$ indicate that phonon-phonon scattering (i.e., Umklapp scattering) is not the primary mechanism responsible for the large difference in κ_L between the heat-treated specimens [14]. Normally, phonon-phonon scattering dominates at temperatures above the Debye temperature in thermoelectric materials, and is described by the following equation [14]:

$$\kappa_L = \frac{(6\pi^2)^{2/3}\underline{M}}{V^{2/3}4\pi^2\gamma^2}\frac{(v_{sound})^3}{T} \quad (5)$$

where V is the atomic volume and $\underline{M}$ is the average atomic mass. According to the $\kappa_L \propto \frac{(v_{sound})^3}{\gamma^2}$ relationship, the smaller v_{sound} (~10 %) and γ (~15 % on average for both methods) of heat-treated $NbCoSn_{0.9}Sb_{0.1}$ than heat-treated NbCoSn hardly affected the κ_L value (~0.9 %) because the two parameters compensate each other, and thus cannot account for the drastic κ_L difference (~30 %) observed experimentally. Similarly, the minor changes in v_{sound} and γ for as-sintered and heat-treated NbCoSn cannot explain the ~50 % increase in κ_L after heat treatment. These findings further support the hypothesis that the microstructural features are the key factors driving changes in κ_L for both NbCoSn and $NbCoSn_{0.9}Sb_{0.1}$ after heat treatment.

2.3. Point defect analysis and structural refinement

We then investigated the influence of various microstructural features on the different κ_L values of heat-treated NbCoSn and $NbCoSn_{0.9}Sb_{0.1}$. However, as discussed below, these differences cannot be fully explained without considering their point defect evolution induced by heat treatment. For instance, while heat-treated $NbCoSn_{0.9}Sb_{0.1}$ exhibited a smaller grain size (270 ± 40 nm) than heat-treated NbCoSn (430 ± 90 nm) (Fig. 1e and f), these grain sizes are unlikely to account for the significantly different κ_L of the two specimens, as the phonon mean free path in most HH compounds is below 100 nm [14,49,50]. In our previous work, we have shown that grain sizes larger than 100 nm have little impact on the κ_L of NbCoSn using the Debye–Callaway model.[28]

Similarly, the variations in the type and concentration of nano-precipitates between the two specimens cannot adequately explain the large difference in κ_L. The observed total number density of nano-precipitates in both specimens, before and after annealing, was approximately 10^{22} m^{-3} (Table S3), which is 100 times lower than the density (1.3×10^{24} m^{-3}) we previously reported as significantly affecting the κ_L of NbCoSn HH compounds [39].

Another possible factor affecting the κ_L is the modification of the grain boundary chemistry and phases [51], which has a great influence on the scattering intensity for both phonons and electrons [17,18,52], or even creates conductive pathways within the materials [29,53]. However, the APT results confirmed that there were no notable changes in grain boundary chemistry before and after heat treatment for both specimens (Fig. S10). Therefore, the observed large differences in κ_L must originate from changes in atomic-scale point defects, which are known to effectively reduce κ_L in HH compounds [14,25,54].

To further investigate this aspect, we examined the evolution of point defect configurations in heat-treated NbCoSn and $NbCoSn_{0.9}Sb_{0.1}$ using high-resolution STEM. To this end, we acquired series of STEM images with 30 and 25 frames, respectively, and used non-rigid registration with bias correction [55] to reconstruct average images. The resulting high-resolution HAADF-STEM images of heat-treated NbCoSn and $NbCoSn_{0.9}Sb_{0.1}$ acquired along the [110] zone axis enable the clear distinction of the different Wyckoff positions without overlap (Fig. 6a and b). According to the ideal structure (without point defects) of NbCoSn viewed along [110], Nb, Sn (Sb), Co atoms, and vacancies

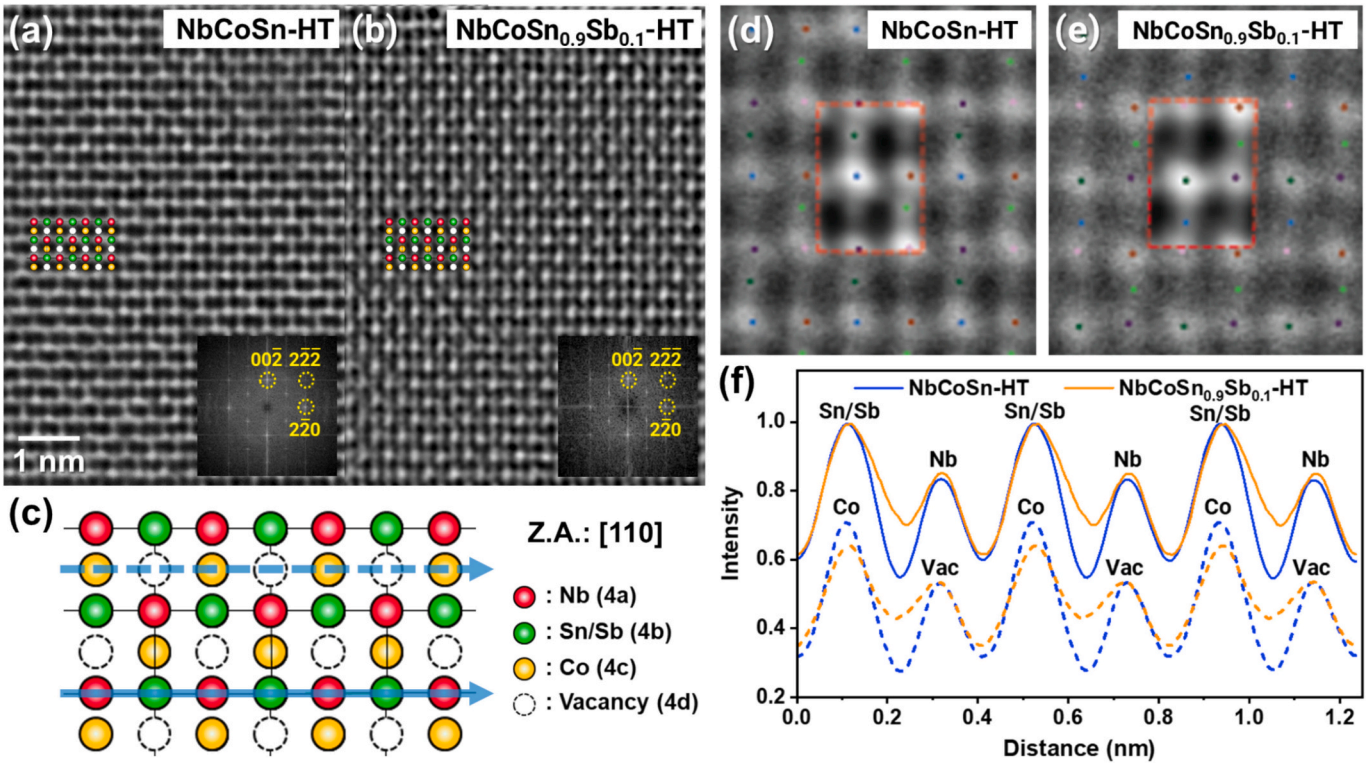

Fig. 6. High-resolution STEM analysis of point defects. HAADF-STEM images of heat-treated (a) NbCoSn and (b) $NbCoSn_{0.9}Sb_{0.1}$. (c) Structural model of NbCoSn along [110] direction, showing different Wyckoff positions. (d,e) Extracted unit cells from the STEM images in (a) and (b), using the direct motif extraction method for heat-treated (d) NbCoSn and (e) $NbCoSn_{0.9}Sb_{0.1}$. (f) Intensity profiles across the 4a/4b (solid lines) and 4c/4d (dotted lines) atomic columns obtained from the unit cells in (d) and (e). All intensity profiles are normalized to the Sn/Sb atomic sites.

occupy the 4a (0,0,0), 4b (1/2, 1/2, 1/2), 4c (1/4, 1/4, 1/4) and 4d (3/4, 3/4, 3/4) Wyckoff positions, respectively (Fig. 6c). The contrast of HAADF-STEM images is proportional to $Z^{1.7–1.9}$ (where Z is the atomic number), allowing for identification of individual atomic columns (Z_{Nb} = 41; Z_{Co} = 27; Z_{Sn} = 50; Z_{Sb} = 51) [56]. To avoid human bias in selecting regions of interest for intensity profiling, averaged unit cell images were generated from each HAADF-STEM image via the direct motif extraction method described by Alhassan et al. [57], while prescribing the number of atoms in the motif to six instead of estimating it automatically. The extracted unit cells represent average intensity distributions for each site within the unit cell, allowing precise comparison of atomic column intensities (Fig. 6d and e). The corresponding intensity profiles across the three atomic column sites and vacancy site obtained from the unit cells are shown in Fig. 6f.

The intensity profile across the 4a/4b columns revealed that heat-treated NbCoSn has slightly lower intensity at the Nb sites, suggesting the presence of Nb vacancies (V_{Nb}) or Co antisite defects (Co_{Nb}). Simulated STEM intensity profiles confirm that both V_{Nb} and Co_{Nb} reduce the Z-contrast at the Nb sites, with V_{Nb} causing a more pronounced reduction (Fig. S11). On the other hand, intensity profiles across the 4c/4d columns revealed a marked difference in the intensity of Co sites between two specimens, while the of intensity of Co vacancy sites was similar. The lower intensity of Co sites observed in the heat-treated $NbCoSn_{0.9}Sb_{0.1}$ suggests a reduced occupancy at these positions, likely due to the migration of Co atoms from the 4c to other sites during heat treatment, resulting in Co vacancies (V_{Co}).

These findings provide insights into the evolution of carrier concentration after heat treatment. In NbCoSn, excess Co typically exists as Co interstitials at 4d vacancy sites (I_{Co}), providing additional electrons by forming mid-gap defect states [40]. The observed decrease in n_H of NbCoSn after heat treatment implies a reduction in I_{Co} amount (Fig. 4b). This explanation is supported by the lower Co concentration revealed by APT and the formation of Co-rich precipitates (Fig. 3h). Notably, $NbCoSn_{0.9}Sb_{0.1}$ exhibited an even greater decrease in n_H after heat treatment. Given the comparable intensity of Co vacancy sites between the two specimens, this further reduction is attributed to acceptor-like V_{Co} in $NbCoSn_{0.9}Sb_{0.1}$.

The point defect distribution in each specimen was further investigated by neutron diffraction experiments on a larger scale. Neutrons have a larger penetration depth than X-rays due to the absence of electrostatic interaction with the electron cloud, and can thus provide accurate information on site occupancies and atomic displacement parameters in materials [58]. Therefore, the average structural disorder over the entire specimen was accurately estimated by Rietveld refinement of the neutron scattering data. Each refinement was performed using a single NbCoSn phase, owing to the low intensities of secondary phases in the diffraction patterns. Based on the APT and STEM measurements, we incorporated I_{Co}, V_{Nb}, Co_{Nb}, and Co vacancies (V_{Co}) in the initial structural model, while Sn- and Sb-related point defects were excluded because their concentrations were close to the nominal values. The Rietveld fits for each specimen matched well with the experimental data (Fig. S12). The detailed refined parameters are provided in Table S4.

The as-sintered NbCoSn exhibited a composition characterized by Nb deficiency and excess Co, which primarily existed as Co_{Nb} antisites rather than I_{Co}, whereas no V_{Co} species were detected (see Table 1). Although I_{Co} has often been often reported as the most energetically favorable defect in NbCoSn, the Nb deficiency likely promoted Co_{Nb} formation over I_{Co} [40]. The preferential occupancy of excess Co at Co_{Nb} sites in NbCoSn has also been reported [26]. As a result, the as-sintered NbCoSn mainly contained V_{Nb} and Co_{Nb} with a minor amount of I_{Co}, yielding a $Nb_{0.85}Co_{1.1}Sn$ composition, consistent with the APT results (Table 1). After heat treatment, the content of point defects was significantly reduced. I_{Co} species were largely eliminated, as the attempts to introduce them led to unrealistically high thermal factors (B_{iso} > 10). The V_{Nb} and Co_{Nb} contents were also reduced, but the V_{Nb} level exhibited a more significant decrease due to its higher formation energy [40]. The remaining excess Co mainly existed as Co_{Nb} (~6.8 %), resulting in a more stoichiometric composition ($Nb_{0.91}Co_{1.06}Sn$). This is also consistent with the APT results and indicates an improved atomic order after heat treatment. Similar results have been reported for NbCoSn [26], (Ti,Hf)Ni(Sn,Sb) [25], and ZrNiSn [59].

On the other hand, $NbCoSn_{0.9}Sb_{0.1}$, displayed unique point defect characteristics before and after heat treatment. In the as-sintered state, it possessed excess Co but no Nb deficiency, indicating that Co occupied interstitial sites (I_{Co}) rather than forming Co_{Nb} antisites. Furthermore, the V_{Co} content was identified to be ~1.6 %, suggesting the formation of Frenkel defects (I_{Co}–V_{Co} pairs) in $NbCoSn_{0.9}Sb_{0.1}$ [14]. After heat treatment, the I_{Co} content decreased by ~50 % but still remained. Simultaneously, Co_{Nb} were newly form with increasing V_{Co} content. This site mixing, in which Co atoms migrate from 4c to 4d sites by heat treatment and Co vacancies are formed at the 4c sites, is consistent with the STEM intensity profiles observed for heat-treated $NbCoSn_{0.9}Sb_{0.1}$ (Fig. 6f). Moreover, the refinement results showed that Co atoms can also migrate to 4a sites, thereby forming Co_{Nb} antisites. Compared to heat-treated NbCoSn, heat-treated $NbCoSn_{0.9}Sb_{0.1}$ exhibits a similar concentration of Co_{Nb}; however, V_{Nb} is only observed in heat-treated NbCoSn. This observation is also in good agreement with the STEM results (Fig. 6f). Consequently, $NbCoSn_{0.9}Sb_{0.1}$ exhibited increased disorder after heat treatment, compared to the improved atomic ordering in NbCoSn. The similar Co excess and slight Nb reduction after heat treatment are also consistent with the APT results.

2.4. Effect of point defect evolution on lattice thermal conductivities

The evolution of point defects plays a substantial role in the observed differences in κ_L between NbCoSn and $NbCoSn_{0.9}Sb_{0.1}$ after heat treatment. In NbCoSn, the increase in κ_L can be attributed to the removal of I_{Co}, $V_{Nb,}$ and Co_{Nb} species. However, in $NbCoSn_{0.9}Sb_{0.1}$, although the I_{Co} content was slightly reduced after heat treatment, Co migration led to an alternative evolution of V_{Co} and Co_{Nb}, which helped to maintain a low κ_L (~4 W m^{-1} K^{-1}). To support this hypothesis, we used the Debye–Callaway model, incorporating point defects contents derived from Rietveld refinement (see Supplementary text and Table S5). Indeed, point defect scattering effectively closed the gap between experimental and calculated κ_L values when only Umklapp, grain boundary, and nano-precipitate scattering were considered (Fig. 7). The κ_L calculated by including point defect scattering closely matched the experimental κ_L for all specimens. Although the effect of point defect scattering was reduced for NbCoSn after heat treatment, it increased in the case of

Table 1
Point defect concentrations and compositions for NbCoSn and $NbCoSn_{0.9}Sb_{0.1}$ obtained from Rietveld refinement of neutron diffraction data. The compositions determined by APT are also included for comparison.

Defect (%)	NbCoSn	NbCoSn-HT	$NbCoSn_{0.9}Sb_{0.1}$	$NbCoSn_{0.9}Sb_{0.1}$-HT
V_{Nb}	6.86	1.89	–	–
I_{Co}	1.63	0	7.20	3.36
Co_{Nb}	8.38	6.84	–	7.03
V_{Co}	–	–	1.61	4.07
Composition (Neutron)	$Nb_{0.85}Co_{1.10}Sn$	$Nb_{0.91}Co_{1.07}Sn$	$NbCo_{1.06}Sn_{0.9}Sb_{0.1}$	$Nb_{0.94}Co_{1.05}Sn_{0.9}Sb_{0.1}$
Composition (APT)	$Nb_{0.86}Co_{1.1}Sn_{1.04}$	$Nb_{0.88}Co_{1.08}Sn_{1.04}$	$NbCo_{1.05}Sn_{0.85}Sb_{0.1}$	$Nb_{0.96}Co_{1.04}Sn_{0.9}Sb_{0.1}$

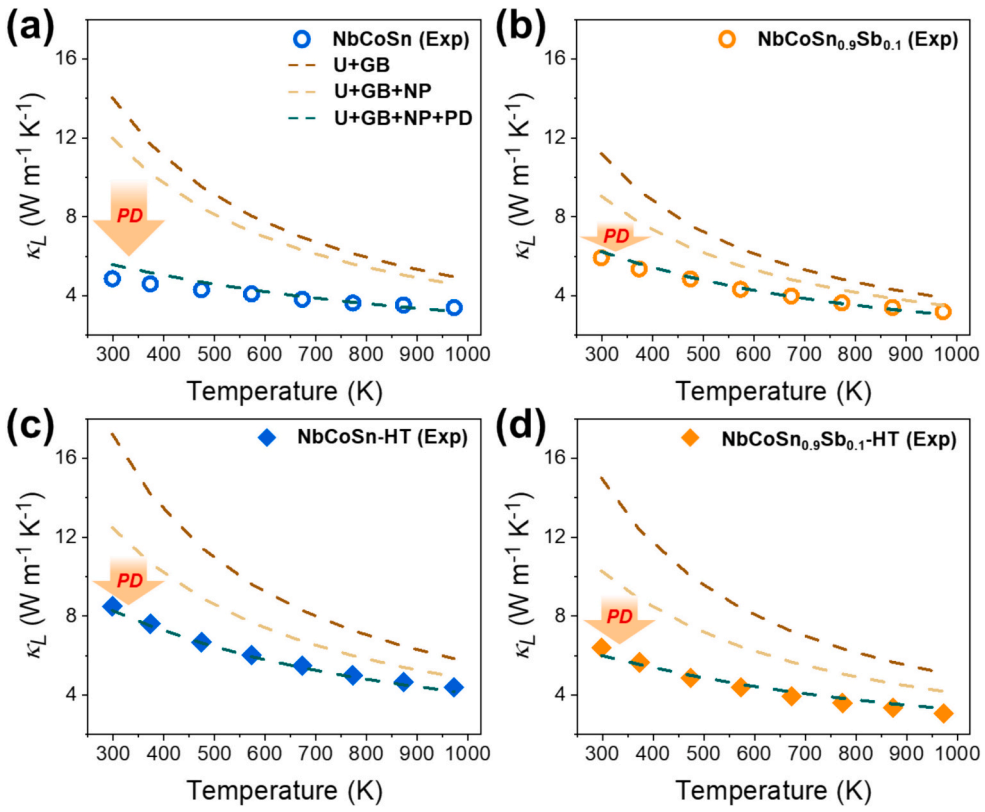

Fig. 7. Critical role of point defects on κ_L calculated by Debye–Callaway model. Experimental (symbols) vs. calculated (dashed lines) κ_L corresponding to different scattering mechanisms for as-sintered (a) NbCoSn, (b) $NbCoSn_{0.9}Sb_{0.1}$ as well as heat-treated (c) NbCoSn and (d) $NbCoSn_{0.9}Sb_{0.1}$. U, GB, NP, and PD denote Umklapp, grain boundary, nanoprecipitate, and point defect scattering, respectively.

$NbCoSn_{0.9}Sb_{0.1}$, owing to the compensating impact of point defect evolution, as shown in Table 1. These results validate the point defect concentrations obtained from neutron diffraction and highlight the critical role of the point defect evolution on the thermal stability of $NbCoSn_{0.9}Sb_{0.1}$ under heat treatment.

Interestingly, while we expected heat-treated $NbCoSn_{0.9}Sb_{0.1}$ to contain a higher concentration of V_{Nb} or Co_{Nb} as suggested by the greater intensity contrast between the 4a and 4b columns in the STEM images, the refinement unexpectedly revealed a higher concentration of these defects in the heat-treated NbCoSn. This discrepancy may result from point defect clustering. Previous studies on TiNiSn and ZrNiSn have demonstrated that Ni interstitials and Ni/Co antisite defects can form local clusters, creating nanodomains within the matrix, as confirmed through DFT calculations and TEM analyses [25,60–62]. Our findings suggest a similar correlation between I_{Co} and Co_{Nb} in $NbCoSn_{0.9}Sb_{0.1}$. Such clustered defects could explain the pronounced intensity difference between 4a and 4b columns in $NbCoSn_{0.9}Sb_{0.1}$, whereas in NbCoSn, the Co_{Nb} and V_{Nb} defects are more randomly distributed and less localized in the imaged area. Further investigation of these local defect domains through a combination of APT and theoretical simulations could yield valuable insights for future studies [63].

Furthermore, these results suggest that even a small amount of Sb can significantly alter the formation energy of point defects, likely by modifying the bonding characteristics and local electronic structures. This change affects the point defect configurations after heat treatment and enhances the thermal stability of NbCoSn and $NbCoSn_{0.9}Sb_{0.1}$. To support this hypothesis, we performed DFT calculations for NbCoSn and $NbCoSn_{0.97}Sb_{0.03}$, focusing on the dependence of the site mixing energy (E_{mix}) of Co atoms on Sb doping.

The site mixing of Co atoms between the 4c and 4d sites was analyzed by calculating the energy difference before and after moving one Co atom from a 4c to a 4d site in both systems. The E_{mix} value was determined using the following equation:

$$E_{mix} = E_{Co\ at\ 4c\ and\ 4d} - E_{Co\ at\ 4c} \quad (6)$$

where $E_{Co\ at\ 4c\ and\ 4d}$ denotes the total energy of NbCoSn or $NbCoSn_{0.97}Sb_{0.03}$ with one Co atom at a 4c site moved to a 4d site, while $E_{Co\ at\ 4c}$ represents the energy of the system with all Co atoms confined to 4c sites. The calculations were conducted for 2 × 2 × 2 supercells containing 96 atoms with a varying distance between the Sb and Co atoms at the 4d site (Fig. S13). Within the chosen supercells, the site mixing energies when Co relocated to the 1st and 2nd nearest neighbor 4d site to the Sb atom were 3.45 and 3.37 eV, showing that moving to the 2nd nearest neighbor 4d site is energetically most favorable. The results show that the E_{mix} for $NbCoSn_{0.97}Sb_{0.03}$ is lower than that of NbCoSn (3.67 eV), confirming that Sb doping facilitated the site mixing of Co atoms between 4c and 4d sites (Fig. 8). This finding demonstrates the critical role of Sb in promoting defect configurations that contribute to the enhanced thermal stability of $NbCoSn_{0.9}Sb_{0.1}$.

3. Conclusion

In this work, we investigated the effects of Sb doping on the thermal stability of NbCoSn by conducting long-term heat exposure experiments on NbCoSn and $NbCoSn_{0.9}Sb_{0.1}$ at 973 K for 1 week. While NbCoSn showed significant thermal degradation in terms of zT, $NbCoSn_{0.9}Sb_{0.1}$ exhibited minimal degradation, primarily due to their different changes in κ_L after heat treatment. Through a combination of multiscale analyses, we identified the point defect evolution as the key factor influencing their different thermal stabilities. Heat treatment largely eliminated point defects in NbCoSn, whereas in $NbCoSn_{0.9}Sb_{0.1}$, the reduction in I_{Co} was compensated by site mixing of Co and Co_{Nb} antisites. This complementary point defect evolution preserved the lattice thermal conductivity of $NbCoSn_{0.9}Sb_{0.1}$ under prolonged heat exposure, as

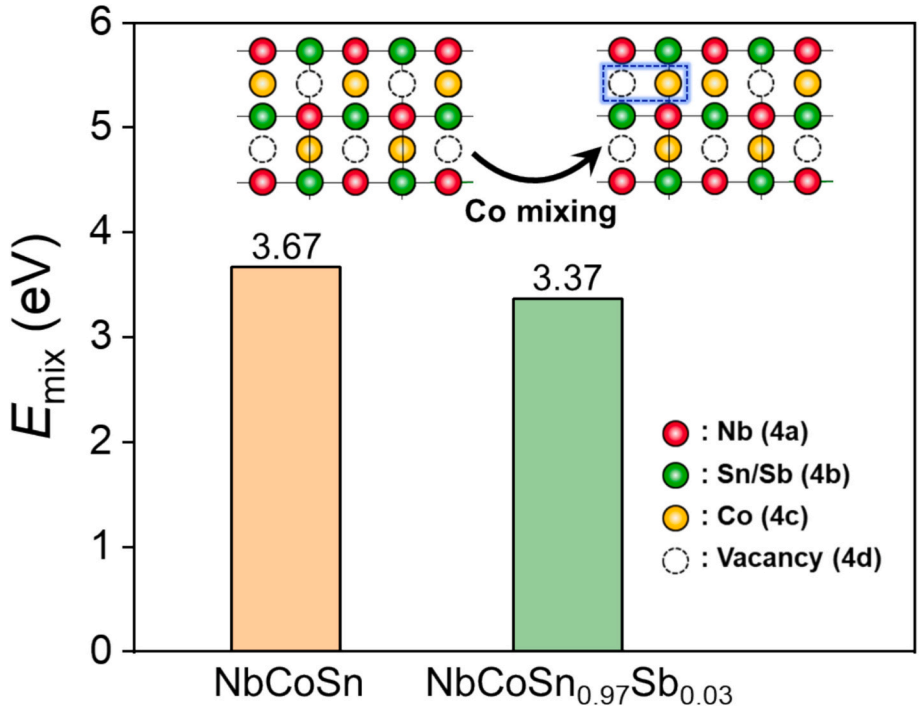

Fig. 8. Calculated site mixing energies (E_{mix}) of Co between 4c and 4d sites for NbCoSn and $NbCoSn_{0.97}Sb_{0.03}$ using density functional theory. The schematic illustration shows the site mixing process of Co atom between 4c and 4d sites.

corroborated by the Debye–Callaway model. Our findings highlight the broad impact of dopants in the defect distribution by altering the distribution and evolution of point defects during heat treatment. This work provides a deeper understanding of the process–structure–property relationships for HH compounds and highlights the potential of defect engineering through tailored dopants to enhance both the performance and long-term reliability of thermoelectric materials.

4. Experimental section

4.1. Fabrication of sintered specimens

Ingots with NbCoSn and $NbCoSn_{0.9}Sb_{0.1}$ target composition (at.%) were prepared by vacuum arc melting under a high-purity Ar (> 99.999 %) atmosphere using high-purity elements (Nb, Co > 99.95 %, Sn > 99.99 %). Additional Sn (~2 wt%) was introduced to compensate for its loss due to its low melting point. Each alloy was remelted five times to ensure chemical homogeneity during the casting. To fabricate amorphous ribbons (~20 μm in thickness and ~ 500 μm in width), we used the melt-spinning technique: the ingots were re-melted in a quartz tube and ejected through a nozzle onto a rotating Cu wheel at a speed of 40 m s^{-1}. The obtained ribbons were crushed into fine powders by using a planetary ball mill (Nano Ceratech NCTP-05 L) for 10 h at 150 rpm (1.6 g), with a ball-to-powder ratio of 15:1. The obtained powders were sintered in a spark plasma sintering machine (Fuji Electronic industrial model SPS-515S) at a temperature of 953 K for 5 min under a load of 50 MPa in vacuum.

4.2. Structural characterization and STEM simulation

Structural analyses were performed by X-ray diffractometer (RIGAKU SmartLab) operated at 45 kV and 200 mA, with monochromatic Cu Kα radiation at 0.01° step size. Inductively coupled plasma–optical emission spectrometry (ICP-OES) (Thermo Fisher Scientific ICAP 6500) was used to measure the chemical compositions of the as-melted ribbons. A dual-beam focused ion beam (FIB)–SEM system (FEI Helios 450 F1) was used to fabricate specimens for APT. APT analyses were carried out using a local electrode atom probe (LEAP 4000× HR, CAMECA Instrument) in pulsed laser mode at 50 K. The laser pulse energy and frequency were set to 50 pJ and 125 kHz, respectively. Data reconstruction and analyses were carried out with the IVAS 3.8.2 software provided by CAMECA Instruments. STEM images were captured using a Titan Themis probe-corrected microscope operated at 300 kV. HAADF-STEM images were acquired with a collection angle of 73–200 mrad. STEM-EDS imaging was conducted using a SuperX detector. Multivariate statistical analysis was employed to denoise the spectrum images [64]. HAADF-STEM image simulations were performed using QSTEM software, employing the same measurement parameters as experiments. Direct motif extraction from high-resolution STEM images was performed using the open-source code available at https://github.com/berkels/msiplib. Methodological details are provided in [57].

Nanoindentation experiments were conducted using a KLA G200 nanoindenter equipped with a diamond Berkovich tip. Indents were made to a maximum depth of 300 nm, ensuring consistent depths across both specimens. Measurements were performed at room temperature using the continuous stiffness measurement (CSM) method, which provided hardness (H) and elastic modulus (E) values as a function of the penetration depth. The maximum allowable drift rate was set to 0.05 nm s^{-1}, with a fixed load rate of 0.05 s^{-1}. The H and E values were extracted using the Oliver and Pharr method [65].

Sound velocities were measured using the pulse-echo technique, with the transducer serving as both the source and receiver of the pulse signal. For measurements, an ultrasonic pulse receiver (DPR 300, JSR Ultrasonic), a longitudinal transducer (CMR-052, ndtXducer), and a normal shear incidence transducer (SM-052, ndtXducer) were utilized. A digital oscilloscope (DSO-X 2022 A, Keysight) displayed the waveform. The time intervals between echoes were recorded to determine the ultrasound reflection time delay, and the sound velocity was then calculated using the formula: $v=2d/t$, where t represents the time delay and d is the sample thickness.

Neutron diffraction measurements for NbCoSn and $NbCoSn_{0.9}Sb_{0.1}$ specimens were carried out on the HRPD beamline at the HANARO

research reactor of the Korea Atomic Energy Research Institute (KAERI). Vertically collimated incident neutrons were monochromated to wavelengths of 1.834530 and 1.834528 Å for as-sintered and heat-treated specimens, respectively, using a single-crystal Ge (331) monochromator. Data were collected over a 2θ range of 10° to 160° with a step size of 0.05° at room temperature. For measurement, each specimen was enclosed in an airtight vanadium can with approximate dimensions of 8 mm in diameter and 50 mm in length.

4.3. Measurements of thermoelectric properties

Sintered specimens were cut into bars ($2 \times 2 \times 9$ mm^3) and disks (Φ 12.7 × 2 mm^3) for electronic and thermal transport property measurements, respectively. The S and σ values were measured at 298–973 K in helium atmosphere using a commercial instrument (Ulvac ZEM-3) [66]. Room-temperature Hall measurements were performed using a physical property measurement system (PPMS, Quantum Design). Thermal conductivities were calculated from the equation $\kappa = DC_p\,\rho$. Thermal diffusivities (D) were measured by a laser flash method (Netzsch LFA-457). Specific heat (C_p) values were obtained from reported data [21]. Densities (ρ) were measured by a He gas pycnometer (Micromeritics AccuPyc II 1340). The zT values were calculated as $zT = S^2\sigma\kappa^{-1}T$. The combined uncertainty for the experimental determination of zT was about 15–20 %, due to the measurements of σ, S, D, C_p, and ρ [67,68].

4.4. DFT calculations

First-principles DFT calculations [69,70] were performed at 0 K using the Vienna ab initio simulation package (VASP) [71]. To calculate site mixing energies, we used $2 \times 2 \times 2$ supercells comprising 96 atoms. Total energies and forces were calculated using the projector augmented-wave method [72] along with the generalized gradient approximation for the exchange-correlation potential parametrized by Perdew, Burke, and Ernzerhof [73]. Single-electron wavefunctions were expanded in plane waves up to an energy cutoff of 500 eV. Structural optimization of bulk NbCoSn and $NbCoSn_{0.97}Sb_{0.03}$ was performed using the tetrahedron method [74] with an $8 \times 8 \times 8$ k-point grid. An energy tolerance of 10^{-7} was employed as convergence criterion for the self-consistent electronic loop. All atomic positions and lattice vectors were relaxed until the residual forces acting on each atom were below 0.0001 eV Å^{-1}. Such strict choices of cutoff parameters and convergence criteria yielded DFT energies with an error $\leq$ 0.1 meV atom^{-1}.

CRediT authorship contribution statement

Kyuseon Jang: Writing – review & editing, Writing – original draft, Methodology, Investigation, Formal analysis, Conceptualization. **Poulumi Dey:** Methodology, Investigation. **Biswanath Dutta:** Methodology, Investigation. **Hail Park:** Investigation. **Ji-Hee Son:** Investigation. **Jeong-In Jang:** Investigation. **Mohammed Kamran Bhat:** Investigation. **Hanhwi Jang:** Investigation. **Hyungsub Kim:** Investigation. **Jungwoo Choi:** Investigation. **Siyuan Zhang:** Investigation. **Ruben Bueno Villoro:** Investigation. **Benjamin Berkels:** Investigation. **Bongseo Kim:** Investigation. **Pyuck-Pa Choi:** Investigation. **Min-Wook Oh:** Investigation. **Yeon Sik Jung:** Investigation. **Jeong Woo Han:** Investigation. **Christina Scheu:** Writing – review & editing, Supervision, Funding acquisition. **Chanwon Jung:** Writing – review & editing, Writing – original draft, Supervision, Funding acquisition, Conceptualization.

Declaration of competing interest

The authors declare that they have no known competing financial interests or personal relationships that could have appeared to influence the work reported in this paper.

Acknowledgement

This work was supported by Basic Science Research Program through the National Research Foundation of Korea (NRF) (grant number RS-2024-00359650 and 2021R1A6A3A03045488). C.J. acknowledges the Global Joint Research Program funded by Pukyong National University (202411890001). S.Z., B.B., and C.S. acknowledge funding from the Deutsche Forschungsgemeinschaft (DFG) within the Collaborative Research Center SFB 1394 “Structural and Chemical Atomic Complexity—From Defect Phase Diagrams to Materials Properties” (Project ID 409476157, project groups B01, A04).

Appendix A. Supplementary data

Supplementary data to this article can be found online at https://doi.org/10.1016/j.cej.2025.164845.

Data availability

The data that support the findings of this study are available from the corresponding author upon reasonable request.

References

[1] G.J. Snyder, E.S. Toberer, Complex thermoelectric materials, Nat. Mater. 7 (2008) 105–114, https://doi.org/10.1038/nmat2090.
[2] C. Zhou, Y.K. Lee, Y. Yu, S. Byun, Z.-Z. Luo, H. Lee, B. Ge, Y.-L. Lee, X. Chen, J. Y. Lee, Polycrystalline SnSe with a thermoelectric figure of merit greater than the single crystal, Nat. Mater. 20 (2021) 1378–1384.
[3] S. Roychowdhury, T. Ghosh, R. Arora, M. Samanta, L. Xie, N.K. Singh, A. Soni, J. He, U.V. Waghmare, K. Biswas, Enhanced atomic ordering leads to high thermoelectric performance in AgSbTe2, Science 371 (2021) 722–727.
[4] J. He, T.M. Tritt, Advances in thermoelectric materials research: looking back and moving forward, Science 357 (2017) eaak9997.
[5] S. Chen, Z. Ren, Recent progress of half-Heusler for moderate temperature thermoelectric applications, Mater. Today 16 (2013) 387–395, https://doi.org/10.1016/j.mattod.2013.09.015.
[6] J. Feng, J. Li, R. Liu, Low-temperature thermoelectric materials and applications, Nano Energy 126 (2024) 109651.
[7] R. Basu, A. Singh, High temperature Si–Ge alloy towards thermoelectric applications: a comprehensive review, Mater. Today Phys. 21 (2021) 100468.
[8] K. Jang, W. Ko, J. Son, J. Jang, B. Kim, M. Vega-Parades, H. Jang, M. Allahyari, S. Kim, K. Ryou, Impact of hierarchical dopant-induced microstructure on thermoelectric properties of p-type Si-Ge alloys revealed by comprehensive multi-scale characterization, Adv. Funct. Mater. 34 (2024) 2403785.
[9] B. Jiang, W. Wang, S. Liu, Y. Wang, C. Wang, Y. Chen, L. Xie, M. Huang, J. He, High figure-of-merit and power generation in high-entropy GeTe-based thermoelectrics, Science 377 (2022) 208–213.
[10] O. Meroz, N. Elkabets, Y. Gelbstein, Enhanced thermoelectric properties of n-type Bi2Te3–x se x alloys following melt-spinning, ACS Appl. Energy Mater. 3 (2019) 2090–2095.
[11] H.-T. Liu, Q. Sun, Y. Zhong, Q. Deng, L. Gan, F.-L. Lv, X.-L. Shi, Z.-G. Chen, R. Ang, High-performance in n-type PbTe-based thermoelectric materials achieved by synergistically dynamic doping and energy filtering, Nano Energy 91 (2022) 106706.
[12] D. Ben-Ayoun, Y. Sadia, Y. Gelbstein, Compatibility between Co-metallized PbTe thermoelectric legs and an Ag–Cu–In brazing alloy, Materials (Basel) 11 (2018) 99.
[13] M. Kaller, D. Fuks, Y. Gelbstein, Sc solubility in p-type half-Heusler (Ti1-cScc)NiSn thermoelectric alloys, J. Alloys Compd. 729 (2017) 446–452.
[14] R. He, T. Zhu, Y. Wang, U. Wolff, J.-C. Jaud, A. Sotnikov, P. Potapov, D. Wolf, P. Ying, M. Wood, Z. Liu, L. Feng, N.P. Rodriguez, G.J. Snyder, J.C. Grossman, K. Nielsch, G. Schierning, Unveiling the phonon scattering mechanisms in half-Heusler thermoelectric compounds, Energy Environ. Sci. 13 (2020) 5165–5176, https://doi.org/10.1039/D0EE03014G.
[15] R. He, H. Zhu, J. Sun, J. Mao, H. Reith, S. Chen, G. Schierning, K. Nielsch, Z. Ren, Improved thermoelectric performance of n-type half-Heusler MCo1-xNixSb (M= Hf, Zr), Mater. Today Phys. 1 (2017) 24–30.
[16] C. Fu, T. Zhu, Y. Pei, H. Xie, H. Wang, G.J. Snyder, Y. Liu, Y. Liu, X. Zhao, High band degeneracy contributes to high thermoelectric performance in p-type half-Heusler compounds, Adv. Energy Mater. 4 (2014) 1400600, https://doi.org/10.1002/aenm.201400600.
[17] R.B. Villoro, R.H. Naderloo, D.A. Mattlat, C. Jung, K. Nielsch, C. Scheu, R. He, S. Zhang, Composite design of half-Heusler thermoelectrics: selective doping of grain boundary phases in NbFeSb by InSb, Mater. Today Phys. 38 (2023) 101240.
[18] R. Bueno Villoro, D. Zavanelli, C. Jung, D.A. Mattlat, R. Hatami Naderloo, N. Pérez, K. Nielsch, G.J. Snyder, C. Scheu, R. He, Grain boundary phases in NbFeSb half-Heusler alloys: a new avenue to tune transport properties of thermoelectric materials, Adv. Energy Mater. 13 (2023) 2204321.

[19] R.H. Naderloo, R.B. Villoro, D.A. Mattlat, P. Ying, S. Song, S. Bayesteh, K. Nielsch, C. Scheu, Z. Ren, H. Zhu, Performance advancements in P-type TaFeSb-based thermoelectric materials through composition and composite optimizations, Energy Environ. Sci. 18 (2025) 738–749.

[20] Z. Liu, S. Guo, Y. Wu, J. Mao, Q. Zhu, H. Zhu, Y. Pei, J. Sui, Y. Zhang, Z. Ren, Design of high-performance disordered half-Heusler thermoelectric materials using 18-electron rule, Adv. Funct. Mater. 29 (2019) 1905044.

[21] R. He, L. Huang, Y. Wang, G. Samsonidze, B. Kozinsky, Q. Zhang, Z. Ren, Enhanced thermoelectric properties of n-type NbCoSn half-Heusler by improving phase purity, APL Mater. 4 (2016), https://doi.org/10.1063/1.4952994.

[22] C. Jung, K. Jang, H. Park, J. Jang, H. Jang, B. Kang, K. Park, S. Zhang, R.B. Villoro, S.D. Park, H.J. Ryu, Y.S. Jung, M.W. Oh, C. Scheu, S.H. Yi, P.P. Choi, Enhanced thermoelectric properties of NbCoSn half-Heuslers through in-situ nanocrystallization of amorphous precursors during the consolidation process, J. Mater. Sci. Technol. 165 (2023) 39–48, https://doi.org/10.1016/j.jmst.2023.04.037.

[23] H. Zhu, W. Li, A. Nozariasbmarz, N. Liu, Y. Zhang, S. Priya, B. Poudel, Half-Heusler alloys as emerging high power density thermoelectric cooling materials, Nat. Commun. 14 (2023) 3300.

[24] Y. Yu, C. Zhou, X. Zhang, L. Abdellaoui, C. Doberstein, B. Berkels, B. Ge, G. Qiao, C. Scheu, M. Wuttig, Dynamic doping and Cottrell atmosphere optimize the thermoelectric performance of n-type PbTe over a broad temperature interval, Nano Energy 101 (2022) 107576.

[25] H.J. Lee, K.H. Lee, L. Fu, G. Han, H.-S. Kim, S.-I. Kim, Y.-M. Kim, S.W. Kim, Critical role of atomic-scale defect disorders for high-performance nanostructured half-Heusler thermoelectric alloys and their thermal stability, Acta Mater. 180 (2019) 97–104.

[26] M.L.C. Buffon, G. Laurita, N. Verma, L. Lamontagne, L. Ghadbeigi, D.L. Lloyd, T. D. Sparks, T.M. Pollock, R. Seshadri, Enhancement of thermoelectric properties in the Nb–co–Sn half-Heusler/Heusler system through spontaneous inclusion of a coherent second phase, J. Appl. Phys. 120 (2016) 75104.

[27] F. Serrano-Sánchez, T. Luo, J. Yu, W. Xie, C. Le, G. Auffermann, A. Weidenkaff, T. Zhu, X. Zhao, J.A. Alonso, Thermoelectric properties of n-type half-Heusler NbCoSn with heavy-element Pt substitution, J. Mater. Chem. A 8 (2020) 14822–14828.

[28] P. Ying, R.B. Villoro, A. Bahrami, L. Wilkens, H. Reith, D.A. Mattlat, V. Pacheco, C. Scheu, S. Zhang, K. Nielsch, Performance degradation and protective effects of atomic layer deposition for Mg-based thermoelectric modules, Adv. Funct. Mater. 34 (2024) 2406473.

[29] T. Luo, F. Serrano-Sánchez, H. Bishara, S. Zhang, R. Bueno Villoro, J.J. Kuo, C. Felser, C. Scheu, G.J. Snyder, J.P. Best, G. Dehm, Y. Yu, D. Raabe, C. Fu, B. Gault, Dopant-segregation to grain boundaries controls electrical conductivity of n-type NbCo(Pt)Sn half-Heusler alloy mediating thermoelectric performance, Acta Mater. 217 (2021) 117147, https://doi.org/10.1016/j.actamat.2021.117147.

[30] Y. Yu, C. Zhou, S. Zhang, M. Zhu, M. Wuttig, C. Scheu, D. Raabe, G.J. Snyder, B. Gault, O. Cojocaru-Mirédin, Revealing nano-chemistry at lattice defects in thermoelectric materials using atom probe tomography, Mater. Today 32 (2020) 260–274, https://doi.org/10.1016/j.mattod.2019.11.010.

[31] S. He, A. Bahrami, C. Jung, X. Zhang, R. He, Z. Ren, S. Zhang, K. Nielsch, Precision interface engineering of CuNi alloys by powder ALD toward better thermoelectric performance, Adv. Funct. Mater. 34 (2024) 2314457.

[32] J.U. Rahman, S. Guo, N. Pérez, K. Jang, C. Jung, P. Ying, C. Scheu, D. Zavanelli, S. Zhang, A. Sotnikov, Grain boundary engineering enhances the thermoelectric properties of Y2Te3, Adv. Energy Mater. 15 (2024) 2404243.

[33] J.C. Slater, Atomic radii in crystals, J. Chem. Phys. 41 (1964) 3199–3204.

[34] D.A. Ferluccio, R.I. Smith, J. Buckman, J.-W.G. Bos, Impact of Nb vacancies and p-type doping of the NbCoSn–NbCoSb half-Heusler thermoelectrics, Phys. Chem. Chem. Phys. 20 (2018) 3979–3987.

[35] C. Zhang, X. Geng, B. Chen, J. Li, A. Meledin, L. Hu, F. Liu, J. Shi, J. Mayer, M. Wuttig, Boron-mediated grain boundary engineering enables simultaneous improvement of thermoelectric and mechanical properties in N-type Bi2Te3, Small 17 (2021) 2104067.

[36] R. Yan, Synthesis, defect tuning, and thermoelectric properties of NbCoSn and ZrNiSn half-Heusler compounds, 2022.

[37] Y. Kimura, Y. Tamura, T. Kita, Thermoelectric properties of directionally solidified half-Heusler compound NbCoSn alloys, Appl. Phys. Lett. 92 (2008) 2–5, https://doi.org/10.1063/1.2828713.

[38] R. Yan, W. Xie, B. Balke, G. Chen, A. Weidenkaff, Realizing p-type NbCoSn half-Heusler compounds with enhanced thermoelectric performance via Sc substitution, Sci. Technol. Adv. Mater. 21 (2020) 122–130.

[39] C. Jung, S. Zhang, K. Jang, N. Cheng, C. Scheu, S.-H. Yi, P.-P. Choi, Effect of heat treatment temperature on the crystallization behavior and microstructural evolution of amorphous NbCo1. 1Sn, ACS Appl. Mater. Interfaces 15 (2023) 46064–46073.

[40] P. Dey, B. Dutta, Decisive role of interstitial defects in half-Heusler semiconductors: an *ab initio* study, Phys. Rev. Mater. 5 (2021) 35407.

[41] C. Jung, B. Dutta, P. Dey, S. Jeon, S. Han, H.-M. Lee, J.-S. Park, S.-H. Yi, P.-P. Choi, Tailoring nanostructured NbCoSn-based thermoelectric materials via crystallization of an amorphous precursor, Nano Energy 80 (2021) 105518, https://doi.org/10.1016/j.nanoen.2020.105518.

[42] J.P. Heremans, V. Jovovic, E.S. Toberer, A. Saramat, K. Kurosaki, A. Charoenphakdee, S. Yamanaka, G.J. Snyder, Enhancement of thermoelectric of the electronic density of states, Science (80-.) 321 (2008) 1457–1461, https://doi.org/10.1126/science.1159725.

[43] G.J. Snyder, A. Pereyra, R. Gurunathan, Effective mass from seebeck coefficient, Adv. Funct. Mater. 32 (2022) 2112772.

[44] G.J. Snyder, A.H. Snyder, M. Wood, R. Gurunathan, B.H. Snyder, C. Niu, Weighted mobility, Adv. Mater. 32 (2020) 2001537.

[45] L. Wu, J. Yang, M. Chi, S. Wang, P. Wei, W. Zhang, L. Chen, J. Yang, Enhanced thermoelectric performance in cu-intercalated BiTeI by compensation weakening induced mobility improvement, Sci. Rep. 5 (2015) 14319.

[46] R. Venkatasubramanian, Lattice thermal conductivity reduction and phonon localizationlike behavior in superlattice structures, Phys. Rev. B 61 (2000) 3091.

[47] E. Isotta, W. Peng, A. Balodhi, A. Zevalkink, Elastic moduli: a tool for understanding chemical bonding and thermal transport in thermoelectric materials, Angew. Chem. 135 (2023) e202213649.

[48] Z. Yang, J. Cao, W. Yu, G. Wang, S. Lang, P. Ding, Effects of microstructure characteristics on the mechanical properties and elastic modulus of a new Ti–6Al–2Nb–2Zr–0.4 B alloy, Mater. Sci. Eng. A, Struct. Mater. Prop. Microstruct. Process. 820 (2021) 141564.

[49] J. Shiomi, K. Esfarjani, G. Chen, Thermal conductivity of half-Heusler compounds from first-principles calculations, Phys. Rev. B (10) (2011) 104302, https://doi.org/10.1103/PhysRevB.84.104302.

[50] C. Jung, S. Jeon, S. Lee, H. Park, S. Han, J. Oh, S.-H. Yi, P.-P. Choi, Reduced lattice thermal conductivity through tailoring of the crystallization behavior of NbCoSn by V addition, J. Alloys Compd. 962 (2023) 171191, https://doi.org/10.1016/j.jallcom.2023.171191.

[51] X. Zhou, P. Mathews, B. Berkels, W. Delis, S. Saood, A. Shamseldeen Ali Alhassan, P. Keuter, J.M. Schneider, S. Korte-Kerzel, S. Sandlöbes-Haut, Materials design by constructing phase diagrams for defects, Adv. Mater. 37 (2025) 2402191.

[52] C. Hu, K. Xia, C. Fu, X. Zhao, T. Zhu, Carrier grain boundary scattering in thermoelectric materials, Energy Environ. Sci. 15 (2022) 1406–1422.

[53] R.B. Villoro, M. Wood, T. Luo, H. Bishara, L. Abdellaoui, D. Zavanelli, B. Gault, G. J. Snyder, C. Scheu, S. Zhang, Fe segregation as a tool to enhance electrical conductivity of grain boundaries in Ti (co, Fe) Sb half Heusler thermoelectrics, Acta Mater. 249 (2023) 118816.

[54] X. Ai, W. Xue, L. Giebeler, N. Pérez, B. Lei, Y. Zhang, Q. Zhang, K. Nielsch, Y. Wang, R. He, Interstitial defect modulation promotes thermoelectric properties of p-type HfNiSn, Adv. Energy Mater. 14 (2024) 2401345.

[55] B. Berkels, C.H. Liebscher, Joint non-rigid image registration and reconstruction for quantitative atomic resolution scanning transmission electron microscopy, Ultramicroscopy 198 (2019) 49–57, https://doi.org/10.1016/j.ultramic.2018.12.016.

[56] T. Saito, F.J.H. Ehlers, W. Lefebvre, D. Hernandez-Maldonado, R. Bjørge, C. D. Marioara, S.J. Andersen, R. Holmestad, HAADF-STEM and DFT investigations of the Zn-containing β ″phase in Al–Mg–Si alloys, Acta Mater. 78 (2014) 245–253.

[57] A.S.A. Alhassan, S. Zhang, B. Berkels, Direct motif extraction from high resolution crystalline STEM images, Ultramicroscopy 254 (2023) 113827, https://doi.org/10.1016/j.ultramic.2023.113827.

[58] J.E. Douglas, P.A. Chater, C.M. Brown, T.M. Pollock, R. Seshadri, Nanoscale structural heterogeneity in Ni-rich half-Heusler TiNiSn, J. Appl. Phys. 116 (2014) 163514.

[59] P. Qiu, J. Yang, X. Huang, X. Chen, L. Chen, Effect of antisite defects on band structure and thermoelectric performance of ZrNiSn half-Heusler alloys, Appl. Phys. Lett. 96 (2010).

[60] D.T. Do, S.D. Mahanti, J.J. Pulikkoti, Electronic structure of Zr–Ni–Sn systems: role of clustering and nanostructures in half-Heusler and Heusler limits, J. Phys. Condens. Matter 26 (2014) 275501.

[61] Y.W. Chai, K. Yoshioka, Y. Kimura, Intrinsic point defects in thermoelectric half-Heusler alloys, Scr. Mater. 83 (2014) 13–16, https://doi.org/10.1016/j.scriptamat.2014.03.025.

[62] X. Yang, Z. Jiang, J. Li, H. Kang, D. Liu, F. Yang, Z. Chen, E. Guo, X. Jiang, T. Wang, Identification of the intrinsic atomic disorder in ZrNiSn-based alloys and their effects on thermoelectric properties, Nano Energy 78 (2020) 105372.

[63] M. He, W.J. Davids, A.J. Breen, S.P. Ringer, Quantifying short-range order using atom probe tomography, Nat. Mater. 23 (2024) 1200–1207.

[64] S. Zhang, C. Scheu, Evaluation of EELS spectrum imaging data by spectral components and factors from multivariate analysis, Microscopy 67 (2018) i133–i141, https://doi.org/10.1093/jmicro/dfx091.

[65] W.C. Oliver, G.M. Pharr, Nanoindentation in materials research: past, present, and future, MRS Bull. 35 (2010) 897–907.

[66] C.J. Perez, M. Wood, F. Ricci, G. Yu, T. Vo, S.K. Bux, G. Hautier, G.M. Rignanese, G. J. Snyder, S.M. Kauzlarich, Discovery of multivalley Fermi surface responsible for the high thermoelectric performance in Yb14MnSb11 and Yb14MgSb11, Sci. Adv. 7 (2021) 1–10, https://doi.org/10.1126/sciadv.abe9439.

[67] H. Wang, S. Bai, L. Chen, A. Cuenat, G. Joshi, H. Kleinke, J. König, H.W. Lee, J. Martin, M.W. Oh, W.D. Porter, Z. Ren, J. Salvador, J. Sharp, P. Taylor, A. J. Thompson, Y.C. Tseng, International Round-Robin study of the thermoelectric transport properties of an n-type half-Heusler compound from 300 K to 773 K, J. Electron. Mater. 44 (2015) 4482–4491, https://doi.org/10.1007/s11664-015-4006-z.

[68] Y. Chen, Z. Ge, M. Yin, D. Feng, X. Huang, W. Zhao, J. He, Understanding of the extremely low thermal conductivity in high-performance polycrystalline SnSe through potassium doping, Adv. Funct. Mater. 26 (2016) 6836–6845.

[69] P. Hohenberg, W. Kohn, Inhomogeneous electron gas, Phys. Rev. 136 (1964) B864–B871, https://doi.org/10.1103/PhysRev.136.B864.

[70] W. Kohn, L.J. Sham, Self-consistent equations including exchange and correlation effects, Phys. Rev. 140 (1965) A1133–A1138, https://doi.org/10.1103/PhysRev.140.A1133.

[71] G. Kresse, J. Hafner, Ab initio molecular dynamics for open-shell transition metals, Phys. Rev. B. 48 (1993) 13115–13118, https://doi.org/10.1103/PhysRevB.48.13115.

[72] P.E. Blöchl, Projector augmented-wave method, Phys. Rev. B. 50 (1994) 17953–17979, https://doi.org/10.1103/PhysRevB.50.17953.
[73] J.P. Perdew, K. Burke, M. Ernzerhof, Generalized gradient approximation made simple, Phys. Rev. Lett. 77 (1996) 3865–3868, https://doi.org/10.1103/PhysRevLett.77.3865.
[74] P.E. Blöchl, O. Jepsen, O.K. Andersen, Improved tetrahedron method for Brillouin-zone integrations, Phys. Rev. B. 49 (1994) 16223–16233, https://doi.org/10.1103/PhysRevB.49.16223.